Diffuse ultrasound computed tomography

Ines Elisa Ulrich, Christian Boehm, Andrea Zunino, et al.

Citation: The Journal of the Acoustical Society of America **151**, 3654 (2022); doi: 10.1121/10.0011540
View online: https://doi.org/10.1121/10.0011540
View Table of Contents: https://asa.scitation.org/toc/jas/151/6
Published by the Acoustical Society of America

ARTICLES YOU MAY BE INTERESTED IN

Finite-element-based resonant ultrasound spectroscopy for measurement of multi-material samples
The Journal of the Acoustical Society of America **151**, 3633 (2022); https://doi.org/10.1121/10.0011516

Green's functions for a layered high-contrast acoustic media
The Journal of the Acoustical Society of America **151**, 3676 (2022); https://doi.org/10.1121/10.0011547

Auditory detection probability of propeller noise in hover flight in presence of ambient soundscape
The Journal of the Acoustical Society of America **151**, 3719 (2022); https://doi.org/10.1121/10.0011546

Source encoding for viscoacoustic ultrasound computed tomography
The Journal of the Acoustical Society of America **147**, 3221 (2020); https://doi.org/10.1121/10.0001191

Acoustic scattering by a small obstacle in the time domain
The Journal of the Acoustical Society of America **151**, 3066 (2022); https://doi.org/10.1121/10.0010449

R. L. Pritchard's classic mutual impedance contribution
The Journal of the Acoustical Society of America **151**, R13 (2022); https://doi.org/10.1121/10.0011507

ASA

Advance your science and career
as a member of the
ACOUSTICAL SOCIETY OF AMERICA

LEARN MORE

JASA ARTICLE

Diffuse ultrasound computed tomography

Ines Elisa Ulrich,[a] Christian Boehm, Andrea Zunino, Cyrill Bösch, and Andreas Fichtner
Department of Earth Sciences, Eidgenössische Technische Hochschule Zürich, Zürich CH-8092, Switzerland

ABSTRACT:
An alternative approach to acquire transmission travel time data is proposed, exploiting the geometry of devices commonly used in ultrasound computed tomography for medical imaging or non-destructive testing with ultrasonic waves. The intent is to (i) shorten acquisition time for devices with a large number of emitters, (ii) to eliminate the calibration step, and (iii) to suppress instrument noise. Inspired by seismic ambient field interferometry, the method rests on the active excitation of diffuse ultrasonic wavefields and the extraction of deterministic travel time information by inter-station correlation. To reduce stochastic errors and accelerate convergence, ensemble interferograms are obtained by phase-weighted stacking of observed and computed correlograms, generated with identical realizations of random sources. Mimicking an imaging setup, the accuracy of the travel time measurements as a function of the number of emitters and random realizations can be assessed both analytically and with spectral-element simulations for phantoms mimicking the model parameter distribution. The results warrant tomographic reconstructions with straight- or bent-ray approaches, where the effect of inherent stochastic fluctuations can be made significantly smaller than the effect of subjective choices on regularisation. This work constitutes a first conceptual study and a necessary prelude to future implementations. © *2022 Acoustical Society of America*.
https://doi.org/10.1121/10.0011540

(Received 3 January 2022; revised 22 April 2022; accepted 13 May 2022; published online 2 June 2022)

[Editor: Keith A. Wear] Pages: 3654–3668

I. INTRODUCTION

Being cost-efficient and free of ionizing radiation, ultrasound tomography is an imaging modality that receives increasing attention in medicine but also in civil engineering. The potential of using transmission ultrasound to infer the structure and to additionally derive the material properties of an unknown medium has been exploited since World War II in non-destructive testing (Desch *et al.*, 1946; Firestone, 1946). The first application of transmission ultrasound in the medical field followed several decades later when Greenleaf and Johnson (1975), Greenleaf and Bahn (1981), and Glover (1977) demonstrated its effectiveness to image breast tissue. Albeit the imaging target differs greatly when comparing the medical to the non-destructive testing application, challenges that arise along the way are similar in both cases. For instance, acquisition devices should ideally combine optimal safety, high resolution of the obtained tomographic images, and cost effectiveness. The latter also addresses the challenge of limited computational power, which is especially relevant for the medical application and has lead to a stagnation in the development of transmission ultrasound for breast screening after the initial proof-of-concept studies. Only recently ultrasound breast imaging regained momentum through the development of new ultrasound computed tomography (USCT) devices with a large number of emitter-receiver pairs that provide dense angular coverage (Duric *et al.*, 2013; Gemmeke *et al.*, 2017; Malik *et al.*, 2018). Correlating the direct arrivals of the pressure wavefield in a reference medium (typically water) and the tissue of interest provides a set of travel time differences that may be used in a ray-based inversion to constrain sound speed variations. The reference recordings additionally serve as a calibration dataset suppressing the source imprint on the waveforms that would otherwise corrupt the travel time measurements. Although there exist more accurate criteria for first-arrival picking [e.g., Li *et al.* (2009)], the combination of correlation-based travel time measurements and ray-based tomography has the advantage of being robust and efficient. Several studies have shown that this setup may produce sound speed maps of human breast tissue that can be used to delineate malignant from benign cell regions (Ranger *et al.*, 2010; Ruiter *et al.*, 2018) and comparable resolution to MRI images can be achieved with waveform tomography [e.g., Sandhu *et al.* (2015)]. In non-destructive testing, ultrasound imaging is frequently used in concrete evaluation for fault detection, duct localization, and thickness measurement [e.g., Chen *et al.* (2022), Kozlov *et al.* (1997), and Schickert (2005)].

Despite the undeniable success and promise, ultrasound transmission tomography faces several challenges that may affect its further development in both fields of research. Since the acquisition time of a transmission ultrasound dataset scales with the number of emitters, a dense emitter-receiver array that produces the desired high-resolution images may become impractical. For USCT, typical time scales of patient movement impose further restrictions on the acquisition time (Roy *et al.*, 2013). However, by

[a]Electronic mail: ines.ulrich@erdw.ethz.ch

reducing the number of repeated shots, the acquisition time may be shortened at the expense of a decreased signal-to-noise ratio in the resulting stack. Last but not least, the calibration step requires the acquisition of an additional dataset, which complicates the processing, further extends the total acquisition time, and potentially acts as an additional source of errors.

With the primary goals of (i) shortening acquisition time, (ii) suppressing instrument noise, and (iii) eliminating calibration measurements, we investigate an alternative approach whereby travel time information for tomography is extracted from correlations of diffuse ultrasonic wavefields. This is inspired by the approximation of inter-receiver Green's functions by diffuse wavefield correlations that can be shown theoretically [e.g., Claerbout (1968), Lobkis and Weaver (2001), Wapenaar (2003), and Wapenaar and Fokkema (2006)] and experimentally [e.g., Malcolm *et al.* (2004)], and is widely used in seismology to image the Earth's crust and mantle on the basis of ambient seismic noise [e.g., Nakata *et al.* (2019), Sabra *et al.* (2005), Saygin and Kennett (2012), Shapiro *et al.* (2005), and Stehly *et al.* (2009)]. Since ambient ultrasonic wavefields are not available, we propose the generation of a quasi-random wavefield actively which can then be used for the estimation of inter-receiver travel times from cross-correlations of individual recordings. Here, the term "random wavefield" specifically refers to the fact that a diffuse wavefield is characterized by random uncorrelated modal amplitudes with equal variances (in literature, this characteristic is sometimes termed wavefield equipartitioning).

In the following, we derive the relevant equations for Green's function retrieval by diffuse wavefield correlation and present its translation from the large-scale passive seismic setup to a small-scale active setup that may either mimic device geometries for USCT breast cancer screening or common setups used for tomographic imaging of civil engineering objects that contain heavy reinforcement such as pillars. To reduce stochastic errors, we suggest the generation of observed and computed wavefields with identical realizations of random sources, and to accelerate convergence of the ensemble correlations by phase-weighted stacking.

As the simplest proof of concept, we first study a homogeneous medium where a random wavefield can be computed analytically. This serves to estimate the accuracy of travel time estimates. Subsequently, we consider numerically computed random wavefields propagating through a heterogeneous medium, which we then reconstruct tomographically using both straight- and bent-ray algorithms. We conclude with a discussion of the advantages and disadvantages of the method, which should outline the niche within which it may be beneficial.

In the civil engineering context, attempts to use the entire signal and not only the first arriving pulses by coda wave interferometry have been made by Larose and Hall (2009) and Niederleithinger *et al.* (2018) and point at an existing niche for this technique. In the medical field, however, the current absence of USCT devices that could implement random wavefield interferometry makes this work a first conceptual study and a necessary prelude to future practical considerations.

This work makes an effort to provide reproducible science as introduced by the Stanford Exploration Project. Figures labeled [R] are reproducible using codes and input files provided (Ulrich *et al.*, 2022).

II. THEORY

To set the stage, we consider a setup where the domain of interest Ω consists of a water bath with the immersed human breast enclosed by a transducer array, which holds the ultrasonic transducers and delineates the boundary of the domain. For an angular frequency ω, the acoustic pressure $p(\mathbf{x},\omega)$ at position $\mathbf{x}$ is related to the speed of sound $c(\mathbf{x})$ and mass density $\rho(\mathbf{x})$ of the medium by the acoustic wave equation

$$\frac{\omega^2}{\rho(\mathbf{x})c^2(\mathbf{x})}p(\mathbf{x},\omega)+\nabla\cdot\left(\frac{1}{\rho(\mathbf{x})}\nabla p(\mathbf{x},\omega)\right) = -\frac{1}{\rho(\mathbf{x})}f(\mathbf{x},\omega), \tag{1}$$

where the volumetric force density gradient $f(\mathbf{x},\omega)$ of the emitting transducers acts as external source. Neumann, Dirichlet or absorbing boundary conditions may be enforced along different parts of the domain boundary, depending on the specifics of a particular setup. We further assume that the medium is at rest prior to the action of the sources.

A. Diffuse wavefield interferometry

To derive the relevant equations for Green's function retrieval by diffuse wavefield correlation, we borrow an argument from the normal-mode theory by Weaver and Lobkis (2004). A collection of alternative derivations may be found in Fichtner and Tsai (2019). As a starting point, we expand the jth realization of a random pressure wavefield $p_j(\mathbf{x},\omega)$ into the normal modes $\phi_n(\mathbf{x})$ of the acoustic wave operator as

$$p_j(\mathbf{x},\omega)=\sum_n a_{j,n}(\omega)\phi_n(\mathbf{x}), \tag{2}$$

where $a_{j,n}(\omega)$ are the frequency-dependent expansion coefficients or modal amplitudes computed as (see the Appendix)

$$a_m(\omega)=-\frac{1}{(\omega^2-\omega_m^2)}\int_\Omega\frac{1}{\rho(\mathbf{x})}\phi_m^*(\mathbf{x})f(\mathbf{x},\omega)d\mathbf{x}. \tag{3}$$

The normal modes form a complete basis, satisfy the boundary conditions and are orthonormal under a weighted inner product, which is detailed in the Appendix. Using Eq. (2), the cross correlation interferogram $C_j(\mathbf{x}_A,\mathbf{x}_B,\omega)$ between the recordings of the jth realization of the diffuse wavefield

at positions $\mathbf{x}_A$ and $\mathbf{x}_B$ can be written as a double sum over normal modes,

$$\begin{aligned} C_j(\mathbf{x}_A,\mathbf{x}_B,\omega) &= p_j^*(\mathbf{x}_A,\omega)p_j(\mathbf{x}_B,\omega) \\ &= \left[\sum_n a_{j,n}(\omega)\phi_n(\mathbf{x}_A)\right]^* \\ &\quad\times\left[\sum_m a_{j,m}(\omega)\phi_m(\mathbf{x}_B)\right] \\ &= \sum_n\sum_m a_{j,n}^*(\omega)a_{j,m}(\omega)\phi_n^*(\mathbf{x}_A)\phi_m(\mathbf{x}_B). \end{aligned} \tag{4}$$

Taking the arithmetic mean over N realizations yields the ensemble correlation

$$\begin{aligned} C(\mathbf{x}_A,\mathbf{x}_B,\omega) &= \frac{1}{N}\sum_{j=1}^N C_j(\mathbf{x}_A,\mathbf{x}_B,\omega) \\ &= \frac{1}{N}\sum_{j=1}^N\sum_n\sum_m a_{j,n}^*(\omega)a_{j,m}(\omega)\phi_n^*(\mathbf{x}_A)\phi_m(\mathbf{x}_B) \\ &= \frac{1}{N}\sum_n\sum_m \phi_n^*(\mathbf{x}_A)\phi_m(\mathbf{x}_B)\sum_{j=1}^N a_{j,n}^*(\omega)a_{j,m}(\omega). \end{aligned} \tag{5}$$

With some approximation, the sum over random realizations j in (5) can be eliminated under the assumption of equipartitioning, meaning that modal amplitudes are on average nearly uncorrelated in the sense of

$$\frac{1}{N}\sum_{j=1}^N a_{j,n}^*(\omega)a_{j,m}(\omega) \approx \gamma_n(\omega)\delta_{mn}, \tag{6}$$

with a frequency-dependent average modal power spectrum $\gamma_n(\omega) = (1/N)\Sigma_{j=1}^N|a_{j,n}(\omega)|^2$. Substituting Eq. (6) into Eq. (5) yields a simplified, approximate expression for the ensemble correlation,

$$C(\mathbf{x}_A,\mathbf{x}_B,\omega) \approx \sum_n \gamma_n(\omega)\phi_n^*(\mathbf{x}_A)\phi_n(\mathbf{x}_B). \tag{7}$$

Equation (7) may be compared to the normal-mode representation of the Green's function between $\mathbf{x}_A$ and $\mathbf{x}_B$ (Gilbert, 1971),

$$G(\mathbf{x}_A,\mathbf{x}_B,\omega) = -\sum_n \frac{1}{(\omega^2-\omega_n^2)}\phi_n^*(\mathbf{x}_B)\phi_n(\mathbf{x}_A), \tag{8}$$

which we derive, for completeness, in the Appendix.

The comparison of Eqs. (7) and (8) reveals the well-known proportionality of the ensemble correlation $C(\mathbf{x}_A,\mathbf{x}_B,\omega)$ to the Green's function $G(\mathbf{x}_A,\mathbf{x}_B,\omega)$ in the frequency domain. The real-valued proportionality factor depends on the modal power spectrum $\gamma(\omega)$, which is controlled by the frequency content and spatial distribution of the wavefield sources. In most cases, $\gamma_n(\omega) \neq (\omega^2-\omega_n^2)^{-1}$, meaning that the ensemble correlation is not exactly equal to the Green's function, even in the hypothetical case of infinitely many realizations. This difference has implications for the measurement of travel time differences for tomographic reconstructions, which we will consider in more detail in Sec. II C.

Importantly, the phases of the active sources that generate the diffuse wavefield are absent from Eq. (7). Hence, the cross correlation eliminates unknown time shifts of the source wavelets, which typically require calibration runs prior to the actual experiment. Furthermore, the accumulation of a sufficiently accurate ensemble correlation may require less acquisition time than the successive firing of all individual sources one by one.

In the following, we focus on the extraction of travel time information from ensemble correlations. For this, we employ the time-domain version of $C(\mathbf{x}_A,\mathbf{x}_B,\omega)$, denoted by $C(\mathbf{x}_A,\mathbf{x}_B,t)$.

B. Practical calculation of correlation functions

In seismology, where noise interferometry is used extensively, diffuse wavefields are generated by ambient sources, such as ocean waves and atmospheric turbulence [e.g., Ardhuin *et al.* (2019), Ardhuin *et al.* (2011), Ermert *et al.* (2017), Gualtieri *et al.* (2019), Igel *et al.* (2021), and Nakata *et al.* (2019)], or anthropogenic activity. Due to the absence of comparable passive sources in small scale ultrasound experiments, we propose to generate random wavefields actively.

For this, all transducers act simultaneously, each transmitting a different random source time function for a time interval of length T. This produces the first random wavefield realization $p_1(\mathbf{x},t)$ and the first set of inter-receiver correlations $C_1(\mathbf{x}_A,\mathbf{x}_B,t)$. Repeating this process N times with new realizations of source time functions, yields the random wavefield realizations $p_2(\mathbf{x},t),\ldots,p_N(\mathbf{x},t)$ and corresponding correlations $C_2(\mathbf{x}_A,\mathbf{x}_B,t),\ldots,C_N(\mathbf{x}_A,\mathbf{x}_B,t)$. The ensemble correlation $C(\mathbf{x}_A,\mathbf{x}_B,t)$ is then defined as the arithmetic mean

$$C(\mathbf{x}_A,\mathbf{x}_B,t) = \frac{1}{N}\sum_{j=1}^N C_j(\mathbf{x}_A,\mathbf{x}_B,t). \tag{9}$$

As demonstrated in Sec. II A, we expect $C(\mathbf{x}_A,\mathbf{x}_B,t)$ to approximate the inter-receiver Green's function $G(\mathbf{x}_A,\mathbf{x}_B,t)$. The travel time between locations $\mathbf{x}_A$ and $\mathbf{x}_B$ may then—for instance—be estimated by picking the maximum amplitude peak in $C(\mathbf{x}_A,\mathbf{x}_B,t)$.

The number of realizations N needed to obtain stable travel time estimates from Eq. (9) may be impractically large. The convergence of $C(\mathbf{x}_A,\mathbf{x}_B,t)$ towards the inter-station Green's function may be accelerated by replacing the linear arithmetic mean in Eq. (9) with the phase-weighted average (Schimmel and Paulssen, 1997; Schimmel *et al.*, 2011)

https://doi.org/10.1121/10.0011540

$$C_{\mathrm{pw}}(\mathbf{x}_A, \mathbf{x}_B, t) = \frac{1}{N} w(\mathbf{x}_A, \mathbf{x}_B, t) \sum_{j=1}^{N} C_j(\mathbf{x}_A, \mathbf{x}_B, t), \tag{10}$$

where the phase weight $w(\mathbf{x}_A, \mathbf{x}_B, t)$ is defined as

$$w(\mathbf{x}_A, \mathbf{x}_B, t) = \frac{1}{N} \left| \sum_{k=1}^{N} e^{i\varphi_k(\mathbf{x}_A, \mathbf{x}_B, t)} \right|^{\nu}. \tag{11}$$

The angle $\varphi_k(\mathbf{x}_A, \mathbf{x}_B, t)$ is the phase of the analytic signal $\tilde{C}_k = C_k + i\mathcal{H}(C_k)$, where $\mathcal{H}$ denotes the Hilbert transform. The exponent ν controls the extent to which coherent phases are emphasised, and is typically chosen between 1 and 3 in order to avoid excessive waveform distortions in this nonlinear averaging procedure. We adopt $\nu = 2$ in all subsequent examples.

An illustrative example for the active generation of random wavefields and inter-receiver correlations is presented in Fig. 1. The transducer configuration is two-dimensional, with sources arranged in a circle of 0.1 m radius. For a duration of 10 ms, the sources simultaneously radiate a random source time function, generated by a random time series, with a maximum frequency of 1 MHz. The receiver positions $\mathbf{x}_A$ and $\mathbf{x}_B$ are at $r = 15$ cm distance, so that the expected arrival time of the direct wave is 0.1 ms for the homogeneous medium with sound speed $c = 1500$ m/s. Figure 1(b) shows linear averages corresponding to Eq. (9) over varying numbers of random wavefield realizations, N, and sources along the two-dimensional (2-D) ring, N_{src}. Comparing $C(\mathbf{x}_A, \mathbf{x}_B, t)$ to the analytical Green's function, given in 2-D by (Igel, 2016)

$$G(r, t) = \frac{1}{2\pi c^2} U\left(t - \frac{|r|}{c}\right)\left(t^2 - \frac{r^2}{c^2}\right)^{-1/2}, \tag{12}$$

with U being the unit step function and $r = \sqrt{(x_A - x_B)^2 + (y_A - y_B)^2}$, one notes—as expected—that the ensemble correlation approaches the analytical Green's function as N and N_{src} increase. The effect of the phase weight, shown in Fig. 1(b), is to accelerate convergence, mostly by suppressing side-lobes around the main pulse.

C. Travel time difference measurements

Errors in the measurement of travel times may result from remaining random fluctuations for a finite number of realization, but also from differences between correlations and Green's functions, explained in Sec. II A. To reduce measurement errors, we propose to estimate travel time differences Δt_{AB} directly instead of trying to measure absolute arrival times in wave pulses with finite frequency content. For this, we first compute ensemble correlations $C_{\mathrm{pw}}(\mathbf{x}_A, \mathbf{x}_B, t; \mathbf{m}^{\mathrm{init}})$ for a plausible initial model vector $\mathbf{m}^{\mathrm{init}}$, which contains the coefficients of a suitably discretized initial slowness distribution, $c^{-1}(\mathbf{x})$. While this may be computationally expensive, it only has to be done once, because $C_{\mathrm{pw}}(\mathbf{x}_A, \mathbf{x}_B, t; \mathbf{m}^{\mathrm{init}})$ can be used as reference for all subsequent tomographic inversions, e.g., on different patients. The arrival time difference of a wave pulse in $C_{\mathrm{pw}}(\mathbf{x}_A, \mathbf{x}_B, t; \mathbf{m}^{\mathrm{init}})$ and its corresponding pulse in the observed random wavefield correlations $C_{\mathrm{pw}}^{\mathrm{obs}}(\mathbf{x}_A, \mathbf{x}_B, t)$ can be estimated robustly by cross correlation (VanDecar and Crosson, 1990),

$$\Delta t_{AB}^{\mathrm{obs}} = \arg\max \int C_{\mathrm{pw}}(\mathbf{x}_A, \mathbf{x}_B, \tau; \mathbf{m}^{\mathrm{init}})\, C_{\mathrm{pw}}^{\mathrm{obs}}(\mathbf{x}_A, \mathbf{x}_B, t + \tau)\, d\tau. \tag{13}$$

In heterogeneous media, a time window may need to be applied in order to isolate the correct pulse. In contrast to

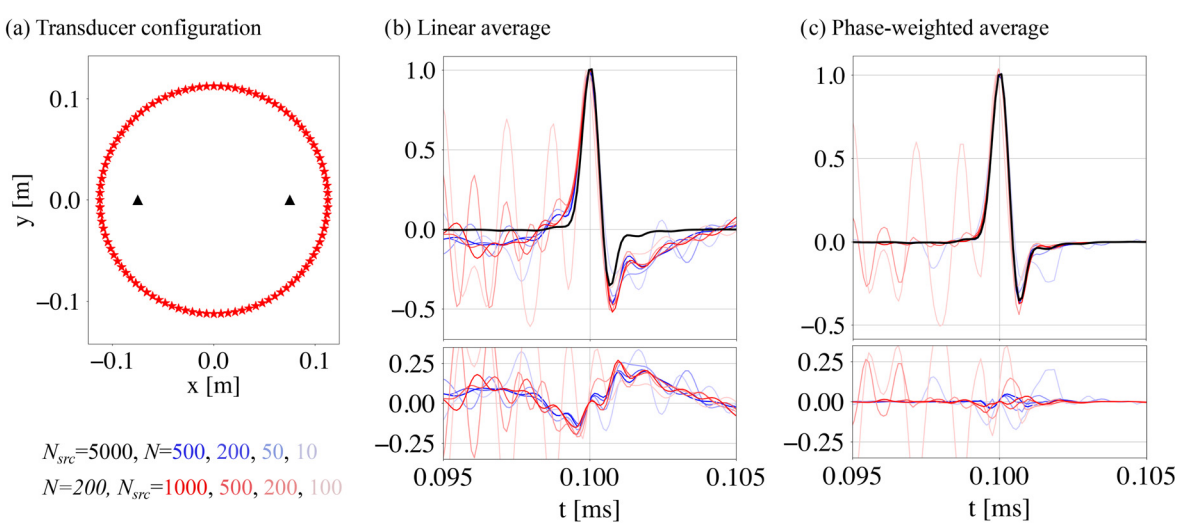

FIG. 1. (Color online) Random wavefield correlations for a 2-D transducer ring. (a) Configuration of sources (red stars) and receivers (black triangles). The sources act simultaneously, each radiating a different random wavelet with a maximum frequency of 1 MHz for the duration of 10 ms, in order to produce one random wavefield realization. (b) Linear averages of the inter-receiver correlation for different numbers of realizations, N, and sources, N_{src}, along the ring. The analytical bandpass-filtered Green's function is plotted in black. The lower panel shows the error, that is, the difference between the analytical Green's function and the ensemble correlations, colour-coded according to the different N and N_{src}. (c) Ensemble correlations similar to panel (b) but for the phase-weighted averaging, according to Eq. (11). The phase weight exponent was set to $\nu = 2$ [R]. (See the Introduction for the reproducibility indicator.)

the picking of individual arrival times, the correlation integral (13) acts to further suppress the influence of incoherent noise. Facilitating tomographic reconstructions, the correlation time shift depends nearly linearly on sound speed variations of up to 10% (Mercerat and Nolet, 2013).

The measurement error in $\Delta t_{AB}^{\mathrm{obs}}$ has three major contributions: (1) noise caused by the instrument itself and by surrounding acoustic sources, (2) convergence failures of the correlation function towards the inter-station Green's function related to the unavoidably finite number of transducers and random wavefield realizations, and (3) random errors caused by the random selection of source-time functions for $C_{\mathrm{pw}}(\mathbf{x}_A, \mathbf{x}_B, t; \mathbf{m}^{\mathrm{init}})$ and $C_{\mathrm{pw}}^{\mathrm{obs}}(\mathbf{x}_A, \mathbf{x}_B, t)$. To eliminate the latter source of errors, we choose identical random realizations of source-time functions for both computed and measured random wavefields. Hence, $C_{\mathrm{pw}}(\mathbf{x}_A, \mathbf{x}_B, t; \mathbf{m}^{\mathrm{init}})$ and $C_{\mathrm{pw}}^{\mathrm{obs}}(\mathbf{x}_A, \mathbf{x}_B, t)$ are directly comparable, regardless of their convergence towards an inter-receiver Green's function.

III. TRAVEL TIME BENCHMARKS

The usefulness of the approach proposed in the previous sections critically relies on the accuracy of travel time difference measurements. Hence, before embarking on a study of tomographic reconstructions in Sec. IV, we analyze travel time differences for a range of different setups. Though such an analysis cannot be exhaustive, it should still point towards useful sets of acquisition parameters.

A. Semi-analytical benchmarks

To assess the performance of the approach proposed in Sec. II under ideal circumstances, we return to the 2-D configuration in Fig. 1 with a homogeneous medium, which allows us to compute Green's functions and random wavefield correlations analytically. Our interest is in the time shift error caused by imperfect convergence towards the Green's function. For this, we compute artificial observations using a homogeneous medium with velocity $c_{\mathrm{obs}} = 1550$ m/s. Given the reference medium with $c = 1500$ m/s and the receiver spacing of 0.15 m, the expected travel time difference is 0.003 22 ms.

The extent to which this travel time difference can be reproduced by the correlation of random wavefield correlations primarily depends on the number of sources N_{src} and the number of realizations N. The latter trades off with the length T of an individual realization, which we fix to 0.1 ms.

Figure 2 summarizes the travel time errors as a function of N_{src} and N for an ensemble of ten independent runs.

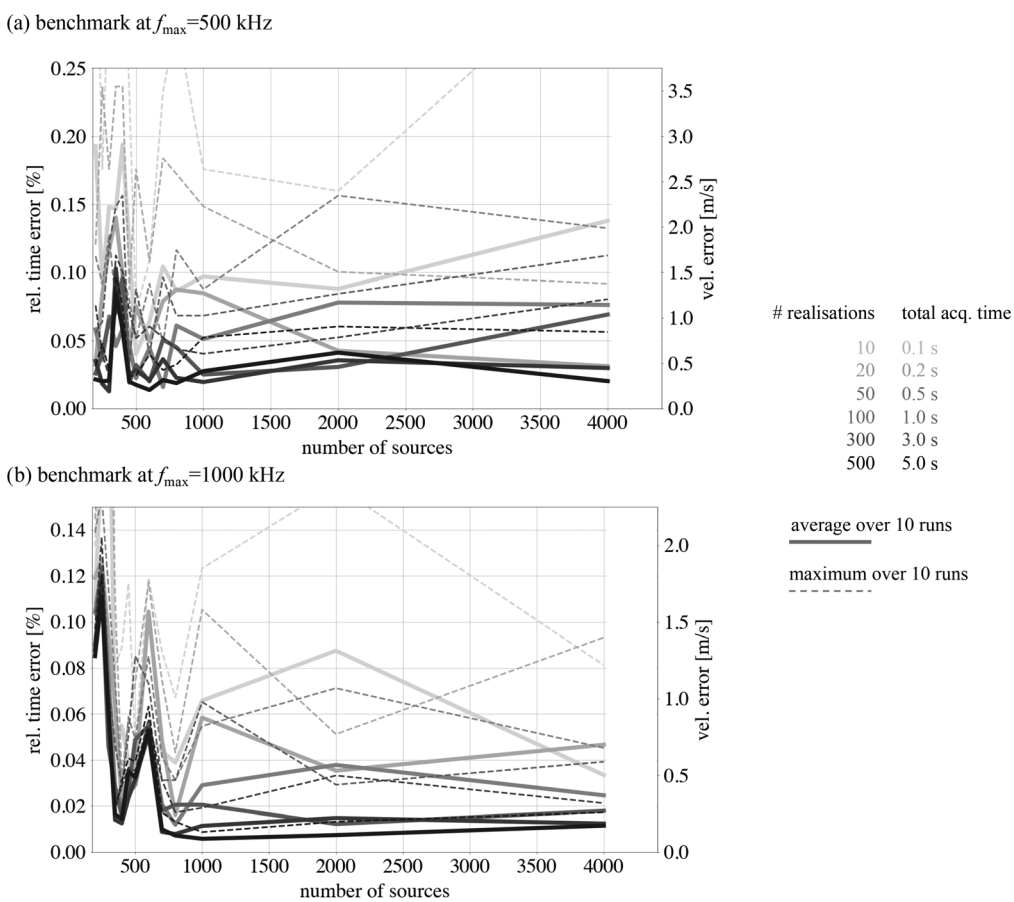

FIG. 2. Errors in the measured travel time difference relative to the travel time of 0.1 ms in the reference medium (left axes), and the corresponding velocity errors (right axes). Different gray shading indicates a variable number of realizations N, ranging from 10 (light gray) to 500 (black). Thick solid curves represent averages over 10 independent runs, and thin dashed curves mark the maximum error within this ensemble. Panel (a) is for a maximum frequency of 500 kHz, and panel (b) for a maximum frequency of 1 MHz [R].

https://doi.org/10.1121/10.0011540

Overall, travel time errors decrease with increasing N_{src} and N. As expected for a stochastic process, where convergence errors are typically proportional to $1/\sqrt{N_{\mathrm{src}}}$, rapid initial error reductions are followed by slower improvements that give the appearance of plateauing when plotted on a linear scale. Furthermore, convergence is not uniform, as specific source configurations produce errors that are larger or smaller. This effect results from systematic differences in convergence speed, which depends on a particular distribution of the discrete wavefield sources within the (higher-order) Fresnel zones. A fortunate configuration will lead to an efficient cancellation of sources outside the stationary-phase region (first Fresnel zone), and vice versa.

As order of magnitude, travel time difference errors relative to the exact travel time of 0.1 s are roughly on the order of 0.05% for a maximum frequency of 500 kHz. The corresponding velocity errors, averaged over the inter-receiver distance of 0.15 m are around 1 m/s. These errors can be reduced by a factor of ∼2 when the maximum frequency is 1 MHz.

Correlation and averaging naturally suppress instrumental noise that is non-propagating and incoherent. This is illustrated in Fig. 3, which displays correlation functions for variable signal-to-noise ratios (SNR) in the artificial observed random wavefields for a scenario with $N_{\mathrm{src}} = 500$ and $N = 100$. Artificial instrumental noise was mimicked by computing realizations of normally distributed Gaussian noise for each time sample, and then adding a lowpass-filtered version with 1 MHz cutoff to the artificial data. A low SNR of 1.5 in the wavefield recordings $p(\mathbf{x}_{A,B})$ leads to an SNR of ∼20 in the inter-receiver correlation $C_{\mathrm{pw}}^{\mathrm{obs}}(\mathbf{x}_A, \mathbf{x}_B)$ and to a relative error in the measured time shift of merely 0.08%. The time shift errors only become more significant when the SNR reaches a level where cycle skips occur. In our example, this happens when the SNR in the observed wavefield is around 0.6.

B. 2D numerical phantom

Taking the semi-analytical implementation described in Sec. II A one step further, we measure travel time shifts for a 2-D heterogeneous phantom, shown in the right panel of Fig. 4. It consists of a circular area with sound speed $c = 1480$ m/s, which is slightly lower than the surrounding values that mimic the water tank. The central part of the phantom contains a low- and and high-speed inclusion. The transducer array with 90 mm radius includes 256 sources that simultaneously act as receivers.

We compute numerical Green's functions between all source-receiver pairs for the heterogeneous phantom using the spectral-element solver Salvus (Afanasiev *et al.*, 2019) in the frequency range of 75 kHz–2 MHz and with absorbing boundaries surrounding the domain. To construct the diffuse wavefield, we convolve the filtered Green's functions with a random source-time function, leading to individual realizations of 0.19 ms duration. Subsequently, we compute inter-receiver correlations and phase weights for all receiver pairs. This process repeats $N = 500$ times, which translates to a total acquisition time of 0.095 s for the phase-weighted ensemble correlations.

The spectral-element simulations of ultrasonic wave propagation ensure accurate solutions for complex numerical phantoms. However, the elevated computational cost also limits the number of scenarios that can be considered.

To establish a baseline, we measure travel time differences between the heterogeneous phantom and the homogeneous reference using actual numerical (spectral-element) Green's functions computed with Salvus. Neglecting small numerical errors, the resulting travel time difference curve, shown in Fig. 4, can serve as ground truth. The corresponding travel time differences obtained through random wavefield interferometry are superimposed in black. They closely follow the baseline, but reveal small fluctuations between neighboring receivers, which we expect from a random process with a finite number of samples. The amplitude of these

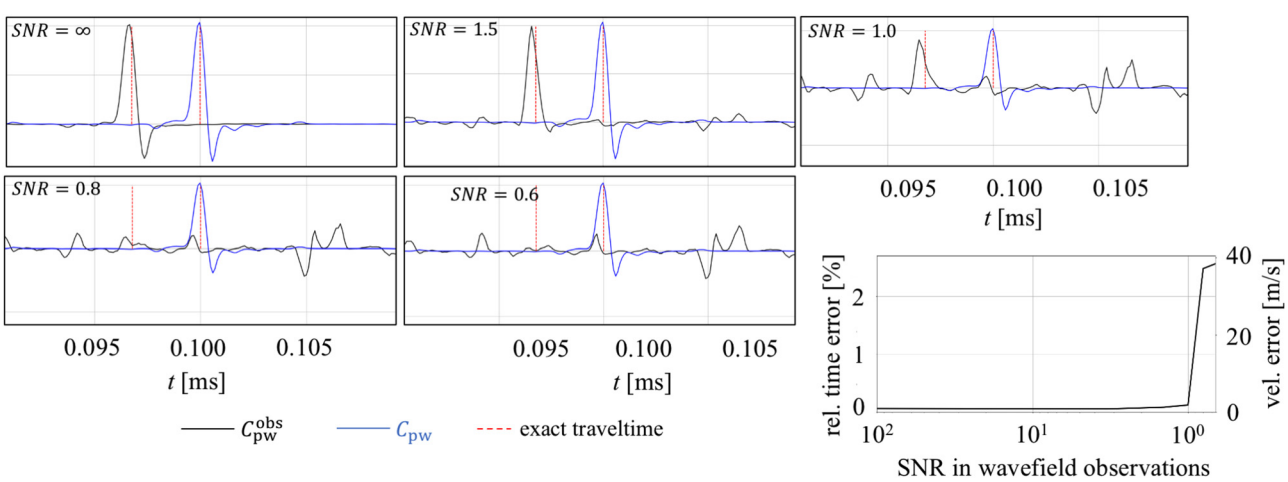

FIG. 3. (Color online) Random wavefield correlations for various signal-to-noise ratios (SNR) in the artificial observed wavefields. Artificial observed correlations are shown in blue, their corresponding computed correlations in black. The panel in the lower right summarizes the relative time shift error and the absolute velocity error as a function of the SNR in the random wavefield observations [R].

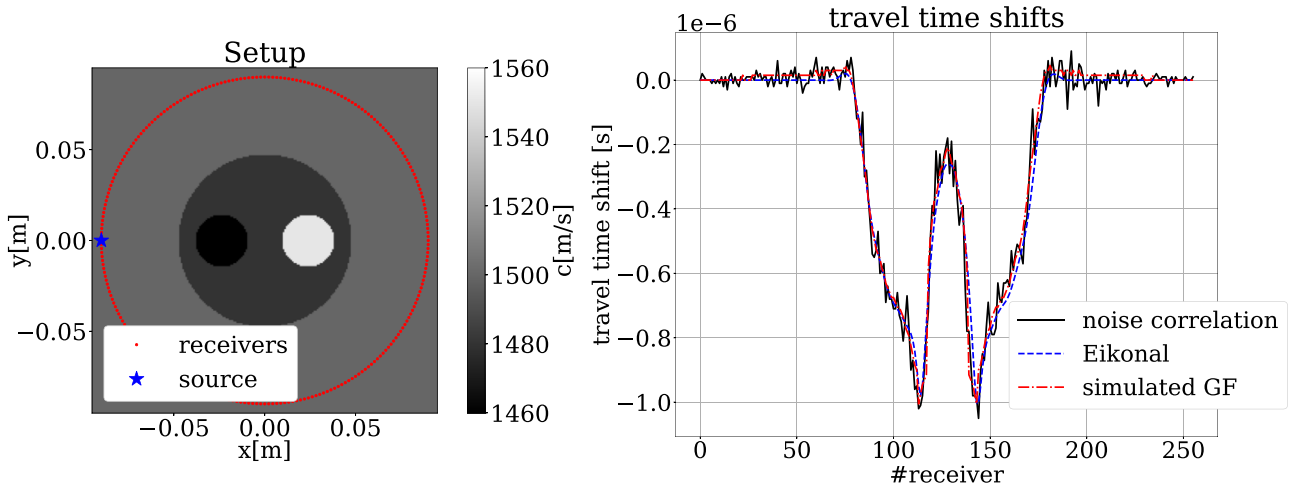

FIG. 4. (Color online) (Left) Setup for the numerical simulations. (Right) Comparison of travel time differences obtained from interferometric cross-correlations (black solid curve), bent-ray simulations (blue dashed curve) and simulations of the full wavefield for the direct Green's functions (red curve) between all receiver pairs and a source located at ⋆.

fluctuations may be reduced by increasing the number of wavefield realizations, and this should be done as a function of the tomographic resolution that one would like to achieve or that is technically achievable with a given number of transducers. As later shown in Sec. IV, the random fluctuations in this example have significantly less impact than subjective choices of regularization.

To complete this analysis, we complement Fig. 4 with a travel time difference curve from a fast-marching solver of the eikonal equation (Rickett and Fomel, 1999; Sethian, 1996). Again, the result closely follows the baseline, as expected. Small systematic differences can, however, be observed at receivers where the corresponding rays travel close to the boundary of a heterogeneity because ray theory ignores the non-zero width of Fresnel zones.

The scale and geometry of the setup mimic common USCT devices, whilst the phantom represents an over simplified version of a 2D cross-sectional slice through a breast. However, in this study, we limit ourselves to this simplified model in order to proof the general concept of diffuse wavefield correlation-based travel time detection. For non-destructive testing on the other hand, the model in Fig. 4 represents the complexity of common imaging targets such as concrete pillars adequately well. However, speed of sound and impedance contrast values would need to be adjusted.

IV. TOMOGRAPHIC INVERSIONS

Equation (1) provides an accurate description of ultrasonic wave propagation in heterogeneous media, and it may be used directly to solve ultrasound full-waveform inversion problems in either the frequency or (after inverse Fourier transform) time domain [e.g., Boehm *et al.* (2018), Calderon Agudo (2017), Pratt *et al.* (2007), and Pérez-Liva *et al.* (2017)]. However, solving the full wave equation repeatedly is computationally challenging, especially in clinical applications. We therefore adopt the ray approximation where space-dependent travel times, $t(\mathbf{x})$, are solutions of the eikonal equation (Cerveny, 2001)

$$|\nabla t(\mathbf{x})^2| = c(\mathbf{x})^{-2}. \tag{14}$$

Equation (14) constitutes the forward problem, the solution of which provides calculated travel time differences $\Delta t_{AB}(\mathbf{m}) = t_{AB}(\mathbf{m}) - t_{AB}^{\text{init}}(\mathbf{m})$ between discretized versions of a variable slowness distribution $\mathbf{m}$ and the initial slowness distribution $\mathbf{m}^{\text{init}}$. To estimate an $\mathbf{m}$ that explains observed travel time differences to within their uncertainties, we minimize the misfit functional

$$J(\mathbf{m}) = \frac{1}{2}\sum_{i,j}\frac{1}{\gamma_{ij}^2}\left[\Delta t_{ij}(\mathbf{m}) - \Delta t_{ij}^{\text{obs}}(\mathbf{m})\right]^2, \tag{15}$$

where the sum is over all contributing virtual source-receivers pairs, and γ_{ij} denotes the standard deviation of the measurement errors, assumed to follow a normal distribution.

Numerical solutions of Eq. (14) can be computed with a variety of methods with different levels of complexity and accuracy, ranging from straight-ray solvers that ignore ray bending, to fast-marching methods that handle strong heterogeneities and shadow zones (Rickett and Fomel, 1999; Sethian, 1996). In the following paragraphs, we will first present a sequence of tomographic reconstructions under the straight-ray approximation. This is intended to highlight the influence of regularization and parametrization. Finally, we employ an eikonal solver that accounts for ray bending, thereby reducing some of the artifacts that result from the straight-ray approximation.

A. Straight-ray tomography

Under the straight-ray approximation, that is, in a perfectly linear regime, the maximum-likelihood model can be obtained by a simple computation of the generalized inverse. Since Fig. 4 indicated that the interferometric travel time

https://doi.org/10.1121/10.0011540

differences are sufficiently accurate to attempt a tomographic reconstruction, we proceed with computing all cross correlation pairs. For this, only one forward simulation with the phantom is required and no calibration data set. Knowing the source and receiver positions, the reference solution for a homogeneous initial model can be computed analytically, and the resulting ensemble correlations can be reused for subsequent tomographic inversions.

In a generic setting, the inverse problem defining the tomographic inversions can be written as

$$\min_{\mathbf{m}} \frac{1}{2}||\mathbf{G}(\mathbf{m}) - \mathbf{d}||_2^2 + \alpha \mathbf{R}(\mathbf{m}), \tag{16}$$

where $\mathbf{G}$ is the forward operator that maps the observables $\mathbf{d}$, which are the time-of-flight differences, to the a specific model $\mathbf{m}$. Due to the non-unique nature of the inverse problem, some form of regularization is required, which is introduced in Eq. (16) through the term $\mathbf{R}(\mathbf{m})$ and the regularization weight α that balances the contributions of data misfits and regularization. In the following, we first consider the linearized forward problem $\mathbf{Gm}$ using the straight-ray-tracing forward operator $\mathbf{G}$ and compare inversion results for three different formulations of the regularization term, namely, damped least squares, second-order Tikhonov regularization and total-variation (TV) regularization. For damped least squares and Tikhonov regularization, the regularization term $\mathbf{R}(\mathbf{m})$ is linear and given explicitly by a matrix, hence a closed-form solution to the inverse problem (16) can be formulated as

$$\tilde{\mathbf{m}} = (\mathbf{G}(\mathbf{m})^T\mathbf{G}(\mathbf{m}) + \alpha \mathbf{R}'(\mathbf{m})^T\mathbf{R}'(\mathbf{m}))^{-1}\mathbf{G}(\mathbf{m})^T\mathbf{d}, \tag{17}$$

where $\mathbf{R}'(\mathbf{m})$ is the derivative of the regularization term with respect to $\mathbf{m}$ defined as $R'_{ij} = (\partial R_i/\partial m_j)$ and $\tilde{\mathbf{m}}$ denotes the optimal model in a least squares sense. Useful levels of regularization can be obtained by examining the trade-off between the solution norm and the residual norm as a function of the regularization weight α as shown in Fig. 5. Acceptable regularization weights are typically found around the kink of the L-curve. Below, we compare the result for four different regularization weightings, indicated in Fig. 5 by the colored dots.

The simple damped least squares formulation applies a damping weight α directly to the model norm, hence $\mathbf{R}(\mathbf{m}) = (1/2)||\mathbf{m}||_2^2$ in Eq. (16). The resulting reconstruction in Fig. 6 already distinguishes the sound speed variations in the numerical phantom. However, the damping penalises deviations from the background medium. This is particularly visible in the lower right panel of Fig. 6, where the strong damping limits the deviation of the sound speed values from the background medium to a small range.

Second-order Tikhonov (smoothing) and total-variation regularization largely circumvent this well-known problem of least squares damping [e.g., Vogel (2002)]. Using second-order Tikhonov, the regularization term applies the ℓ_2 norm to the spatial Hessian with respect to the model parameters, thus, $\mathbf{R}(\mathbf{m}) = (1/2)||\nabla^2\mathbf{m}||_2^2$. The smoothing effect of the spatial Hessian is clearly visible in Fig. 7, where ray artifacts are successfully eliminated by stronger regularization weights. The latter have been chosen on the basis of the L-curve plots in Fig. 5(b).

By design, total-variation regularization successfully reconstructs the discontinuous sound speed distribution of the phantom by penalizing the ℓ_1 norm of the spatial gradient, hence, $\mathbf{R}(\mathbf{m}) = ||\nabla\mathbf{m}||_1$. In the discrete setting, the gradient may be approximated by a first-order finite-difference matrix. For models structured in locally homogeneous regions with discontinuities on their boundaries, the application of a

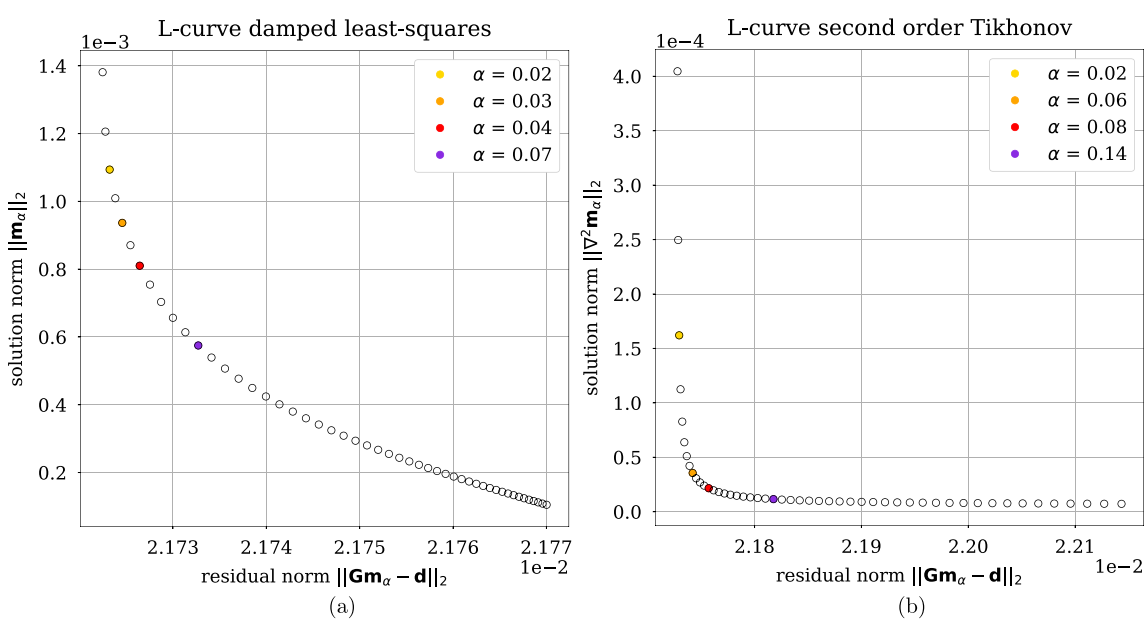

FIG. 5. (Color online) L-curve for damped least squares regularization (a) and Tikhonov regularization (b) using different values of the regularization weight α [R].

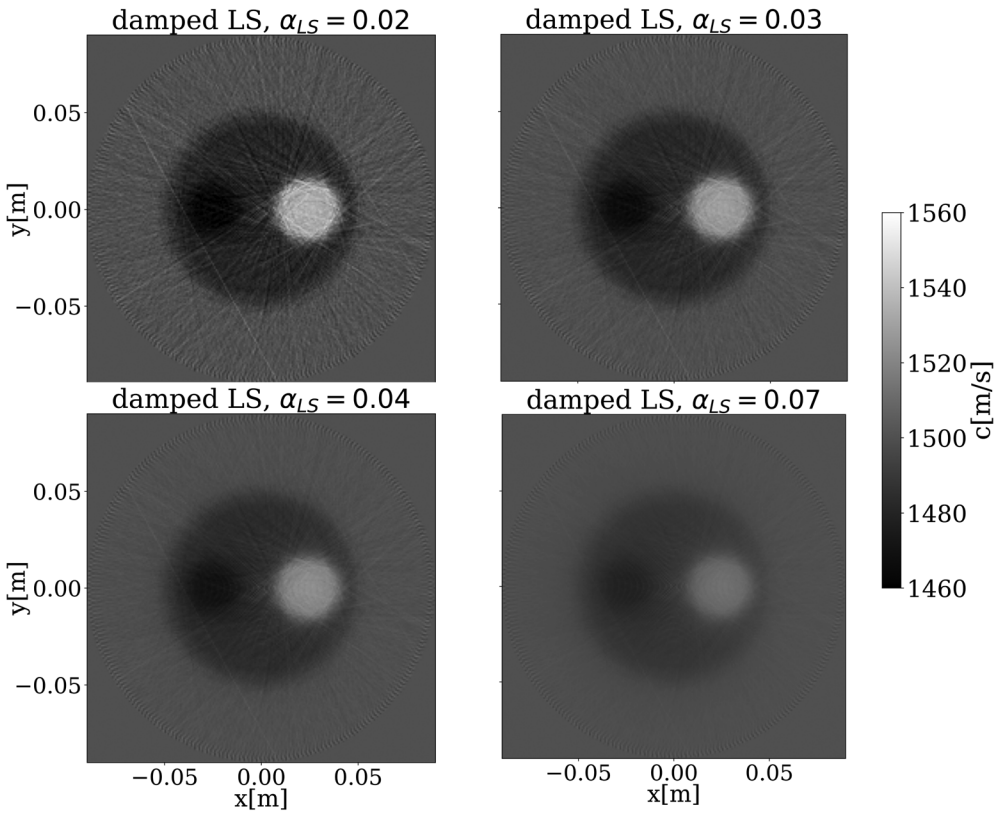

FIG. 6. Reconstructed sound speed maps using damped least squares [R].

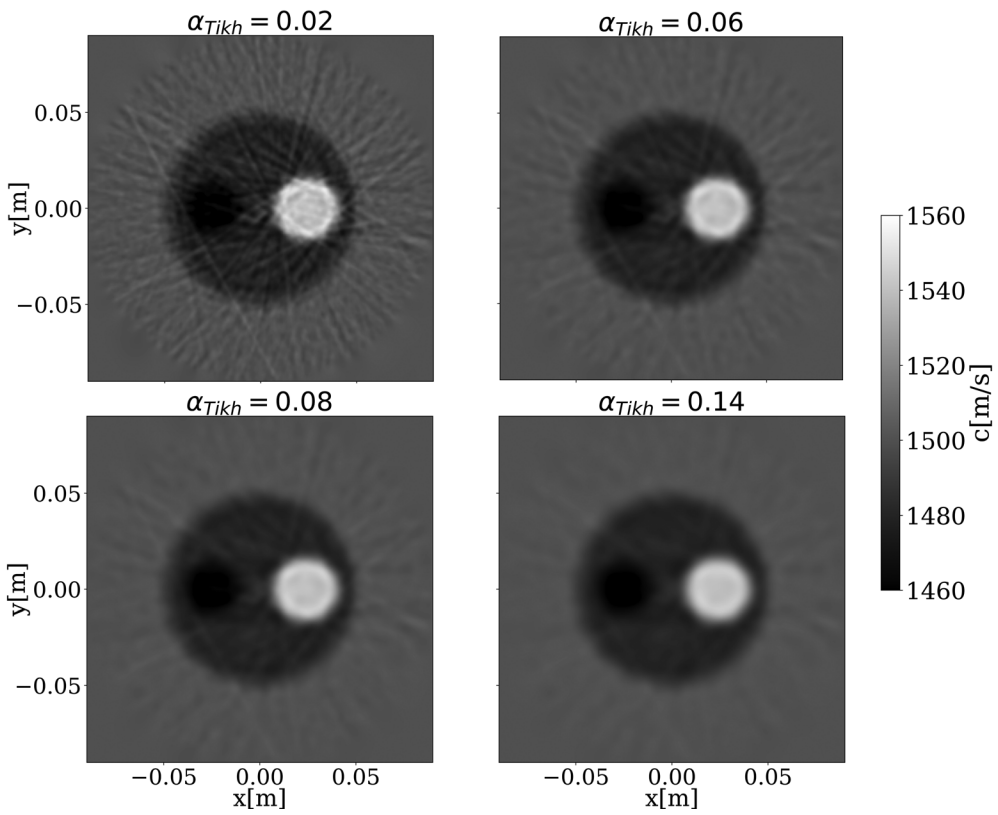

FIG. 7. Reconstructed sound speed maps using second-order Tikhonov regularization for different regularization weightings α_{Tikh} [R].

https://doi.org/10.1121/10.0011540

first-order finite-difference matrix to $\mathbf{m}$ with subsequent summation of the absolute value over all pixels in the grid will result in a gradient only sparsely populated with non-zero values. Hence jumps in the gradient characterizing sharp edges are promoted, which explains the clear delineation of the two inclusions in Fig. 8. To deal with the non-smooth ℓ_1 norm in the regularization term of the total variation formulation, we use the Split-Bregman method (Ravasi and Vasconcelos, 2020), which considers the objective

$$\min_{\mathbf{m}} \frac{1}{2}||\mathbf{G}(\mathbf{m}) - \mathbf{d}||_2^2 + \alpha||\nabla\mathbf{m}||_1. \tag{18}$$

The influence of applying a stronger regularization weight α is especially visible in the upper right plot in Fig. 8, where the piece-wise nature of the phantom is particularly well reconstructed.

The bottom row of Fig. 8 also shows the influence of exploiting the sparsity property of the Fourier basis in the model space. To promote sparse solutions with only a small number of non-zero coefficients in the Fourier space, the transform $\mathbf{Pm}$, where $\mathbf{P}$ is the Fourier operator, enters as ℓ_1 penalty into the objective such that the second term in Eq. (18) reads $\mathbf{R}(\mathbf{m}) = ||\mathbf{Pm}||_1$ (Ulrich *et al.*, 2021). Transforming the problem to a domain where the structure of the medium can be represented by a sparse set of basis functions generally compresses information to a much smaller set of coefficients. However, the lower right plot in Fig. 8, where the regularization contribution is increased in comparison to the lower left plot, shows the stronger influence of the Fourier basis, which is by construction smooth.

B. Bent-ray tomography

In the straight-ray reconstructions, the heterogeneity with high sound speed consistently appears smaller than its neighbor with lower sound speed, even though they have equal size in the phantom. The removal of this artifact requires the incorporation of ray bending, which introduces non-linearity into the inverse problem. Hence, the minimization of the misfit functional J proceeds iteratively, using gradients computed via adjoint techniques [e.g., Sethian and Popovici (1999)] applied to a fast-marching eikonal solver [e.g., Sethian and Popovici (1999)]. To iteratively update $\mathbf{m}$, starting from $\mathbf{m}^{\text{init}}$, we use the L-BFGS algorithm [e.g., Nocedal and Wright (2006)]

$$\mathbf{m}_{k+1} = \mathbf{m}_k - \alpha_k \mathbf{H}_k^{-1} \nabla J(\mathbf{m}_k), \tag{19}$$

where $\mathbf{m}_k$ is the slowness model in the kth iteration, α_k is a step length satisfying the Wolfe condition, $\mathbf{H}_k^{-1}$ is an approximate inverse Hessian of $J(\mathbf{m}_k)$, and $\nabla J(\mathbf{m}_k)$ is the gradient of the misfit functional evaluated at the current model. During each iteration, the approximate inverse Hessian is updated, incorporating new information gained by the model update. Equation (15) together with Eq. (19) describe how travel time difference measurements translate into a velocity model that eventually explains observed data

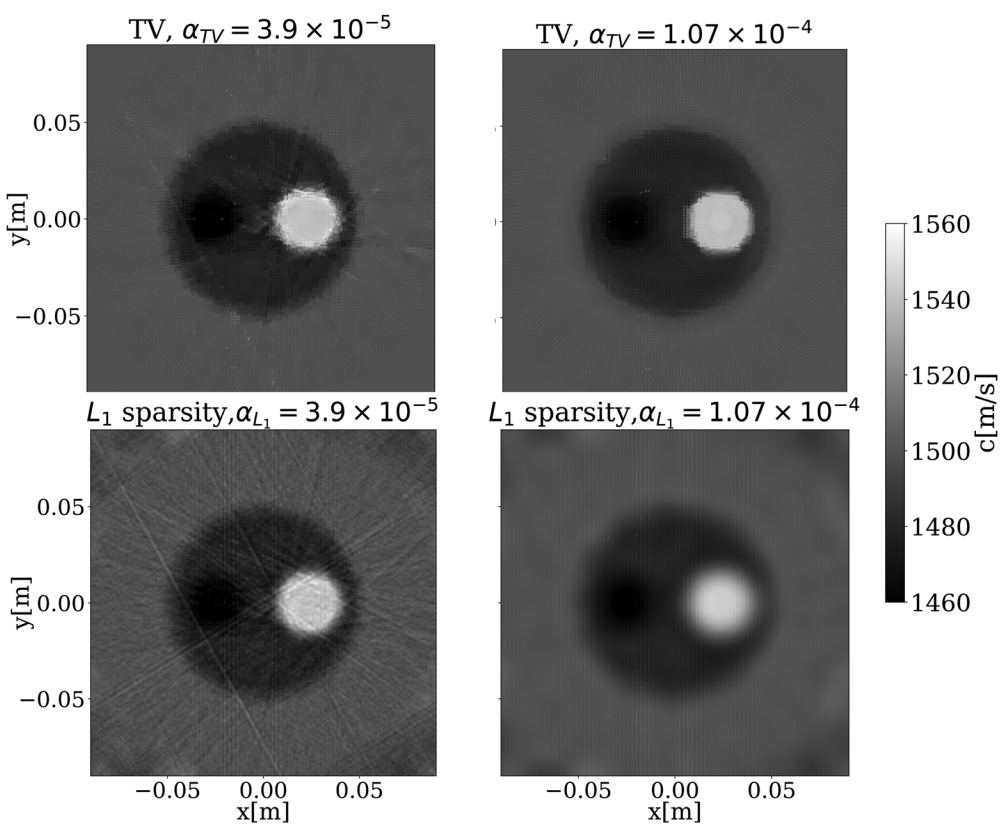

FIG. 8. Reconstructed speed-of-sound maps with TV regularization in pixel space (top row) and a regularization term equal to the ℓ_1 norm applied to the sparse fourier transformed model vector (bottom row) for different values of the regularization weight α [R].

to within the observational errors. We note that there exist algorithms that are computationally more efficient than fast-marching methods, however, the purpose of this example is not to strive for the fastest implementation, but to show the difference between bent- and straight-ray reconstructions.

Figure 9 displays reconstructed sound speed maps using a bent-ray forward model and total-variation regularization after 40 iterations of the L-BFGS algorithm and for different regularization weights. In contrast to the straight-ray reconstructions in Figs. 6–8, the bent-ray forward model successfully reconstructs the sizes of the two inclusions.

V. DISCUSSION

We presented an alternative conceptual approach to USCT that aims to reduce acquisition time and eliminate the calibration step. The main methodological ingredients are the following: (1) Active generation of a diffuse acoustic wavefield by simultaneously acting sources. (2) Computation of ensemble-averaged inter-receiver correlations using phase-weighted stacking. (3) Numerical calculation of reference correlations for an initial sound speed distribution and identical random source realizations as for the real-data acquisition. (4) Estimation of travel time differences by cross correlation and their (iterative) inversion for the sound speed distribution.

In the following, we discuss the niche where the proposed method may be beneficial, as well as key advantages and limitations.

A. Potential savings in acquisition time and scaling of the problem

The relative efficiency of the proposed method primarily depends on its scaling properties, the noise characteristics of the acquisition system, and the desired tomographic resolution. The total acquisition time $\bar{T}_{\text{rand}}$ is

$$\bar{T}_{\text{rand}} = N_{\text{rand}} T_{\text{rand}}, \tag{20}$$

with the number of random wavefield realizations N_{rand} and the duration of an individual realization T_{rand}. By design, $\bar{T}_{\text{rand}}$ is independent of the number of sources N_{src}, in contrast to conventional deterministic approaches where sources act sequentially, leading to a total acquisition time of

$$\bar{T}_{\text{det}} = N_{\text{src}} N_{\text{det}} T_{\text{det}}. \tag{21}$$

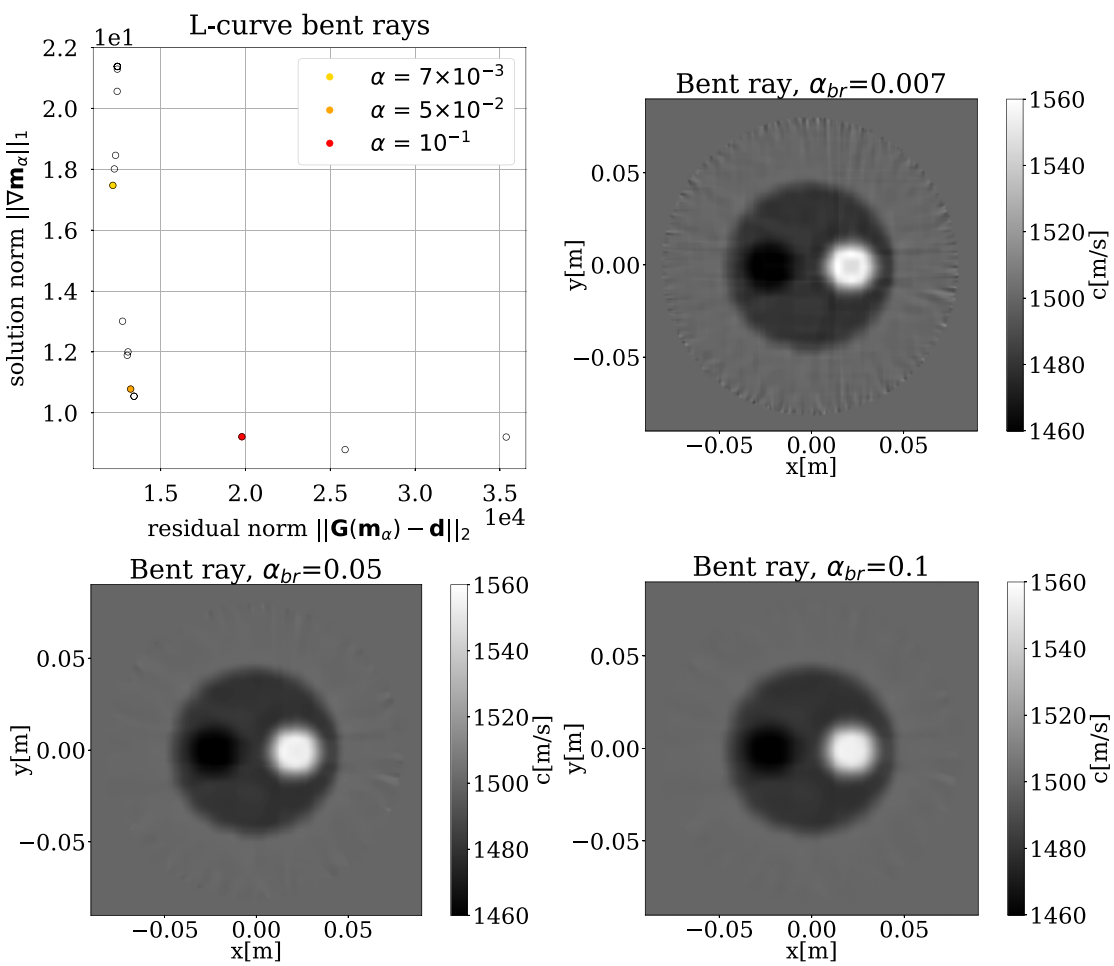

FIG. 9. (Color online) Reconstructed sound speed maps using a bent-ray algorithm that solves the eikonal equation and uses total-variation regularization with three different regularization weights α_{br}.

In Eq. (21), T_{det} denotes the time between subsequent shots, and N_{det} is the number of repetitions, needed to achieve a desired signal-to-noise ratio through stacking. Since the effects of changing T_{rand} and N_{rand} trade-off exactly in the random wavefield approach, we can assume $T_{\mathrm{rand}} = T_{\mathrm{det}}$, without loss of generality, which leads to

$$\frac{\bar{T}_{\mathrm{det}}}{\bar{T}_{\mathrm{rand}}} = N_{\mathrm{src}} \frac{N_{\mathrm{det}}}{N_{\mathrm{rand}}}. \tag{22}$$

Equation (22) states that the random wavefield approach outperforms the sequential deterministic approach when the number of sources is large enough. The precise number of sources where $\bar{T}_{\mathrm{det}}/\bar{T}_{\mathrm{rand}} = 1$ is controlled by the ratio $N_{\mathrm{det}}/N_{\mathrm{rand}}$, which, in turn, depends on the noise characteristics and the desired signal-to-noise ratio.

It follows that an exact assessment of relative efficiency can only be done on an application-specific basis that accounts for the specifics of an actual acquisition system. However, realizing that tomographic resolution ultimately depends on the number of transducers, the random wavefield approach seems to have considerable potential, as we strive to constrain increasingly small sound speed details.

For some USCT systems, passive noise sources such as crosstalk, reverberations and induction of other acoustic modes form coherent background noise that may contribute constructively to the randomness in the signals, which may increase the speed of convergence towards the inter-receiver Green's function in the noise correlations. However, these features are system dependent and hence it is difficult to model these effects generically.

B. Signal-to-noise ratio

As stressed in Sec. V A, the signal-to-noise ratio plays a fundamental role for data quality and scaling properties. Common methods to increase the signal-to-noise ratio include, for instance, averaging over several A-scans or matched filtering, and they may differ for different acquisition systems [e.g., Birk *et al.* (2014)].

Conveniently, the ensemble average correlation, as defined in Sec. IV B, already includes an averaging process, which acts to suppress incoherent instrumental noise. The type of "noise" that is more important for the method presented here is related to insufficient convergence of a stochastic process and the resulting random fluctuations of travel time difference measurements.

C. Elimination of the calibration step

The diffuse wavefield approach transforms each receiver into a virtual source with precisely known properties. It follows that there is no need for calibration runs in a homogeneous medium (typically water) because there is inherently no need to account for system-specific influences such as the angular dependence of the transducers or system delays (Ruiter, 2016). The latter are, in fact, automatically eliminated by the correlation procedure.

The role of a reference is instead being played by the synthetic random wavefield correlations, computed with exact copies of the actual random source realizations for a numerical reference or initial sound speed model. Since reference correlations can be pre-computed once and for all, travel time differences may be inferred directly for any number of patients screened. In a highly optimized clinical routine, which aims at maximum patient throughput, random wavefield interferometry may therefore offer an essential speed-up compared to standard sequential data acquisition.

D. Finite-frequency travel times

The measurement process described in Sec. V C defines an arrival time difference between observed and computed wave pulses with finite frequency content. This is not necessarily identical to an arrival time difference in ray theory, upon which we base our tomographic reconstructions. In fact, ray theory assumes infinite frequencies, which do, however, not exist in numerical simulations or actual experiments.

This discrepancy constitutes a systematic error. It vanishes in the hypothetical case where observed and computed wave shapes are identical, that is, for instance, when the actual and the model medium are homogeneous. Generally avoiding this error, requires the replacement of ray theory by finite-frequency theory, which substitutes infinitely thin rays by volumetrically extended sensitivity kernels that correspond exactly to a certain type of finite-frequency measurement, such as travel time differences by cross correlation (Dahlen *et al.*, 2000; Korta Martiartu *et al.*, 2020; Luo and Schuster, 1991).

Our acceptance of this systematic error is a pragmatic choice. It is justified by the weak heterogeneities within soft tissue, which, being on the order of few percent, generally do not lead to significant distortions of the transmitted wave pulses (Mercerat and Nolet, 2013). Furthermore, the use of finite-frequency theory would increase the computational cost of a tomographic reconstruction by orders of magnitude.

VI. OUTLOOK

This work constitutes a theoretical, and unavoidably simplified, proof of concept of a new USCT approach that we consider a necessary prelude to real-world implementations and there exist variations and adaptations of the method that potentially merit further investigation.

In deterministic sequential acquisition, data coverage is not only controlled by the number of transducers but also by their opening angle. The diffuse wavefield approach, in contrast, may circumvent this limitation because multiple-scattering at the boundaries of the device may eventually produce a nearly equipartitioned wavefield that illuminates the complete medium, independent of the opening angle. With this, it might be possible to increase coverage and potentially tomographic resolution, however, a rigorous test of this effect is beyond the scope of this work, as it would

require the consideration of a range of device geometries in order to produce meaningful results.

The approach of computing synthetic (reference) and observed random wavefields with exact copies of random source realizations carries the potential to go beyond travel time tomography towards waveform tomography. Concerning the medical application for USCT breast cancer screening, where a shift towards waveform reconstruction methods that provide higher spatial resolution has been observed, this extension is indeed an important step to take in further studies in order to highlight the relevance of the presented method. The effectiveness of waveform inversion in the context of non-destructive testing has been studied by Seidl and Rank (2017), who interestingly also point to the connection with medical ultrasound by showing an application of waveform inversion to a human femur.

Using a correlation based misfit measure limits the information available to update the model to the first arriving pulses. Higher order effects are neglected, which in general leads to the fact that ray-based reconstructions are of poorer quality than waveform reconstructions. Especially for realistic breast phantoms with complex interior structure, modelling the effect of multiple scattering correctly is crucial. Since the correlation wavefields by design take into account the finite frequency nature of the signals, they provide all information on finite frequency effects and are thus directly comparable in their entirety. Sager *et al.* (2018) presented a general formulation for waveform ambient noise inversion where the correlation wavefield itself is the solution of the forward problem. This then allows for a waveform reconstruction of the sampled medium that—compared to the presented travel time tomography—inherently models acoustic wave propagation accurately.

ACKNOWLEDGMENTS

The authors would like to thank Guust Nolet for fruitful discussions about finite-frequency travel time measurements using cross-correlation. This work was supported by the Swiss National Supercomputing Centre (CSCS) under project ID s1040.

APPENDIX A: MODAL EXPANSION OF THE GREEN'S FUNCTION

We consider the acoustic wave equation in the frequency domain as introduced in Eq. (1),

$$\frac{\omega^2}{\rho(\mathbf{x})c^2(\mathbf{x})}p(\mathbf{x},\omega)+\nabla\cdot\left(\frac{1}{\rho(\mathbf{x})}\nabla p(\mathbf{x},\omega)\right) = -\frac{1}{\rho(\mathbf{x})}f(\mathbf{x},\omega), \tag{A1}$$

where $p(\mathbf{x},\omega)=\int_{-\infty}^{\infty}p(\mathbf{x},t)e^{-i\omega t}dt$. Depending on the specifics of a particular setup, either Neumann, Dirichlet or absorbing boundary conditions may be enforced along different parts of the domain boundary as

$$p(\mathbf{x},\omega)=0,\quad \mathbf{x}\in\partial\Omega_{\text{Dirichlet}}, \tag{A2}$$

$$\nabla p(\mathbf{x},\omega)\cdot\mathbf{n}(\mathbf{x})=0,\quad \mathbf{x}\in\partial\Omega_{\text{Neumann}}, \tag{A3}$$

where $\mathbf{n}(\mathbf{x})$ is the outward-pointing unit normal. The pressure wavefield $p(\mathbf{x},\omega)$ can be expanded in the normal modes $\phi_n(\mathbf{x})$ of the wave operator as

$$p(\mathbf{x},\omega)=\sum_n a_n(\omega)\phi_n(\mathbf{x}), \tag{A4}$$

where a_n are constants denoting the expansion coefficients, which are physically interpreted as the amplitude. The normal modes of the wave operator form a complete basis of the system that are chosen to satisfy the boundary conditions in Eq. (A3) and that are orthonormal under the weighted inner product defined by

$$\langle\phi_m(\mathbf{x})|\phi_n(\mathbf{x})\rangle=\int_\Omega\frac{1}{\rho(\mathbf{x})c^2(\mathbf{x})}\phi_n^*(\mathbf{x})\phi_m(\mathbf{x})d\mathbf{x}=\delta_{mn}, \tag{A5}$$

where an asterisk means complex conjugation. To find the expansion coefficients a_n in Eq. (A4), we take the weighted inner product of the latter with a mode $\phi_m^*(\mathbf{x})$ and make use of the spatial orthogonality of the modes, which yields

$$\int_\Omega\frac{1}{\rho(\mathbf{x})c^2(\mathbf{x})}\phi_m^*(\mathbf{x})\sum_n a_n(\omega)\phi_n(\mathbf{x})d\mathbf{x} = \sum_n a_n(\omega)\delta_{mn}=a_m(\omega). \tag{A6}$$

Taking the scalar product of Eq. (1) with $\phi_m^*(\mathbf{x})$ and using the expression of the expansion coefficients in Eq. (A6), we get

$$\omega^2 a_m(\omega)+\int_\Omega\phi_m^*(\mathbf{x})\nabla\cdot\left(\frac{1}{\rho(\mathbf{x})}\nabla p(\mathbf{x},\omega)\right)d\mathbf{x} = -\int_\Omega\frac{1}{\rho(\mathbf{x})}\phi_m^*(\mathbf{x})f(\mathbf{x},\omega)d\mathbf{x}. \tag{A7}$$

Equation (A7) is a variational problem, which can be approximated by a finite dimensional problem using the Rayleigh-Ritz method. This allows us to compute the eigenfunctions $\phi_n(\mathbf{x})$ as well as the eigenvalues ω_n^2. Using that the normal mode $\phi_n(\mathbf{x})$ is a solution to the source-free form of the wave equation (1),

$$\frac{\omega_n^2}{\rho(\mathbf{x})c^2(\mathbf{x})}\phi_n(\mathbf{x})+\nabla\cdot\left(\frac{1}{\rho(\mathbf{x})}\nabla\phi_n(\mathbf{x})\right)=0, \tag{A8}$$

we obtain an expression for the volume integral on the left-hand side of Eq. (A7) in terms of the eigenfrequencies ω_n^2 by taking again the scalar product with $\phi_m^*(\mathbf{x})$,

$$\omega_n^2\delta_{mn}=-\int_\Omega\phi_m^*(\mathbf{x})\nabla\cdot\left(\frac{1}{\rho(\mathbf{x})}\nabla\phi_n(\mathbf{x})\right)d\mathbf{x}. \tag{A9}$$

To shift one spatial derivative to $\phi_m^*(\mathbf{x})$, we use integration by parts and exploit that the eigenmodes satisfy the boundary conditions in Eq. (A3),

$$\omega_n^2 \delta_{mn} = \int_\Omega \frac{1}{\rho(\mathbf{x})} \nabla \phi_m^*(\mathbf{x}) \nabla \phi_n(\mathbf{x}) d\mathbf{x}. \tag{A10}$$

Substituting Eq. (A10) into Eq. (A7), we find a representation for the expansion coefficients a_n due to an arbitrary source $f(\mathbf{x}, \omega)$,

$$a_m(\omega) = -\frac{\int_\Omega \frac{1}{\rho(\mathbf{x})} \phi_m^*(\mathbf{x}) f(\mathbf{x}, \omega) d\mathbf{x}}{(\omega^2 - \omega_m^2)}. \tag{A11}$$

Note that each coefficient a_m is weighted by the term $(\omega^2 - \omega_m^2)^{-1}$, comprising the angular frequency ω, resulting from taking the Fourier transform in Eq. (1), and the eigenfrequency ω_m, belonging to a specific eigenmode $\phi_m(\mathbf{x})$. For mathematical convenience, we assume that all eigenmodes have distinct and non-degenerated eigenfrequencies. Inserting the expression for the expansion coefficients in Eq. (2) defines an analytical expression of the modal representation of a pressure wavefield recorded at a position $\mathbf{x}$, due to an arbitrary source field $f(\mathbf{x}, \omega)$,

$$p(\mathbf{x}, \omega) = -\sum_n \frac{\int_\Omega \frac{1}{\rho(\mathbf{x})} \phi_n^*(\mathbf{x}) f(\mathbf{x}, \omega) d\mathbf{x}}{(\omega^2 - \omega_n^2)} \phi_n(\mathbf{x}). \tag{A12}$$

Afanasiev, M., Boehm, C., van Driel, M., Krischer, L., Rietmann, M., May, D. A., Knepley, M. G., and Fichtner, A. (**2019**). "Modular and flexible spectral-element waveform modelling in two and three dimensions," Geophysical J. Int. **216**(3), 1675–1692.

Ardhuin, F., Gualtieri, L., and Stutzmann, E. (**2019**). "Physics of ambient noise generation by ocean waves," in *Seismic Ambient Noise*, edited by N. Nakata, L. Gualtieri, and A. Fichtner (Cambridge University Press, Cambridge, UK), pp. 109–143.

Ardhuin, F., Stutzmann, E., Schimmel, M., and Mangeney, A. (**2011**). "Ocean wave sources of seismic noise," J. Geophys. Res. **116**, C09004, https://doi.org/10.1029/2011JC006952.

Birk, M., Dapp, R., Ruiter, N., and Becker, J. (**2014**). "GPU-based iterative transmission reconstruction in 3D ultrasound computer tomography," J. Parallel Distributed Comput. **74**(1), 1730–1743.

Boehm, C., Korta-Martiartu, N., Vinard, N., Balic, I. J., and Fichtner, A. (**2018**). "Time-domain spectral-element ultrasound waveform tomography using a stochastic quasi-Newton method," SPIE Med. Imag. **2018**, 92–100.

Calderon Agudo, O. (**2017**). "3D imaging of the breast using full-waveform inversion," in *Proceedings of the International Workshop on Medical Ultrasound Tomography*.

Cerveny, V. (**2001**). *Seismic Ray Theory* (Cambridge University Press, Cambridge).

Chen, R., Tran, K., La, H., Rawlinson, T., and Dinh, K. (**2022**). "Detection of delamination and rebar debonding in concrete structures with ultrasonic SH-waveform tomography," Autom. Construction **133**, 104004.

Claerbout, J. F. (**1968**). "Synthesis of a layered medium from its acoustic transmission response," Geophys. **33**(2), 264–269.

Dahlen, F., Hung, S.-H., and Nolet, G. (**2000**). "Fréchet kernels for finite-frequency traveltimes—I. Theory," Geophys. J. Int. **141**, 157–174.

Desch, C., Sproule, D., and Dawson, W. (**1946**). "The detection of cracks in steel by supersonic waves," Iron Steel Inst. **153**(1), 319–327.

Duric, N., Littrup, P., Schmidt, S., Li, C., Roy, O., Bey-Knight, L., Janer, R., Kunz, D., Chen, X., Goll, J., Wallen, A., Zafar, F., Allada, V., West, E., Jovanovic, I., Li, K., and Greenway, W. (**2013**). "Breast imaging with the Softvue imaging system: First results," in *Medical Imaging 2013; Ultrasonic Imaging, Tomography, and Therapy,* edited by J. G. Bosch and M. M. Doyley, (SPIE, Bellingham, WA, 2013), Vol. 8675, pp. 164–171.

Ermert, L., Sager, K., Afanasiev, M., Boehm, C., and Fichtner, A. (**2017**). "Ambient seismic source inversion in a heterogeneous Earth: Theory and application to the Earth's hum," J. Geophys. Res. Solid Earth. **122**, 9184–9207, https://doi.org/10.1002/2017JB014738.

Fichtner, A., and Tsai, V. (**2019**). "Theoretical foundations of noise interferometry," in *Seismic Ambient Noise*, edited by N. Nakata, L. Gualtieri, and A. Fichtner (Cambridge University Press, Cambridge, UK), pp. 109–143.

Firestone, F. A. (**1946**). "The supersonic reflectoscope, an instrument for inspecting the interior of solid parts by means of sound waves," J. Acoust. Soc. Am. **17**(3), 287–299.

Gemmeke, H., Hopp, T., Zapf, M., Kaiser, C., and Ruiter, N. V. (**2017**). "3D ultrasound computer tomography: Hardware setup, reconstruction methods and first clinical results," Nucl. Instrum. Methods Phys. Res. Sect. A **873**, 59–65.

Gilbert, F. (**1971**). "Excitation of the normal modes of the earth by earthquake sources," Geophys. J. R. Astron. Soc. **22**(2), 223–226.

Glover, G. (**1977**). "Computerized time-of-flight ultrasonic tomography for breast examination," Ultrasound Med. Biol. **3**(2), 117–127.

Greenleaf, J., and Johnson, S. (**1975**). "Algebraic reconstruction of spatial distributions of refractive index and attenuation in tissues from time-of-flight and amplitude profiles," in *Proceedings of the Seminar on Ultrasonic Tissue Characterization*, pp. 109–119.

Greenleaf, J. F., and Bahn, R. C. (**1981**). "Clinical imaging with transmissive ultrasonic computerized tomography," IEEE Trans. Biomed. Eng. **BME-28**(2), 177–185.

Gualtieri, L., Stutzmann, E., Juretzek, C., Hadziioannou, C., and Ardhuin, F. (**2019**). "Global-scale analysis and modeling of primary microseisms," Geophys. J. Int. **218**, 560–572.

Igel, H. (**2016**). *Computational Seismology: A Practical Introduction* (Oxford University Press, Oxford).

Igel, J., Ermert, L., and Fichtner, A. (**2021**). "Rapid finite-frequency microseismic noise source inversion at regional to global scales," Geophys. J. Int. **227**, 169–183.

Korta Martiartu, N., Boehm, C., and Fichtner, A. (**2020**). "3-D wave-equation-based finite-frequency tomography for ultrasound computed tomography," IEEE Trans. Ultrason. Ferroelectr. Freq. Control **67**, 1332–1343.

Kozlov, V., Samokrutov, A., and Shevaldykin, V. (**1997**). "Thickness measurements and flaw detection in concrete using ultrasonic echo method," Nondestr. Test. Eval. **13**(2), 73–84.

Larose, E., and Hall, S. (**2009**). "Monitoring stress related velocity variation in concrete with a 2×10^{-5} relative resolution using diffuse ultrasound," J. Acoust. Soc. Am. **125**(4), 1853–1856.

Li, C., Huang, L., Duric, N., Zhang, H., and Rowe, C. (**2009**). "An improved automatic time-of-flight picker for medical ultrasound tomography," Ultrasonics **49**(1), 61–72.

Lobkis, O. I., and Weaver, R. L. (**2001**). "On the emergence of the green's function in the correlations of a diffuse field," J. Acoust. Soc. Am. **110**(6), 3011–3017.

Luo, Y., and Schuster, G. T. (**1991**). "Wave-equation traveltime inversion," Geophysics **56**, 645–653.

Malcolm, A., Scales, J., and Tiggelen, B. (**2004**). "Extracting the green function from diffuse, equipartitioned waves," Phys. Rev. E **70**, 015601.

Malik, B., Terry, R., Wiskin, J., and Lenox, M. (**2018**). "Quantitative transmission ultrasound tomography: Imaging and performance characteristics," Med. Phys. **45**, 3063–3075.

Mercerat, E. D., and Nolet, G. (**2013**). "On the linearity of cross-correlation delay times in finite-frequency tomography," Geophys. J. Int. **192**, 681–687.

Nakata, N., Gualtieri, L., and Fichtner, A. (**2019**). *Seismic Ambient Noise* (Cambridge University Press, Cambridge).

Niederleithinger, E., Wang, X., Herbrand, M., and Müller, M. (**2018**). "Processing ultrasonic data by coda wave interferometry to monitor load tests of concrete beams," Sensors **18**(6), 1971.

Nocedal, J., and Wright, S. (**2006**). *Numerical Optimization: Springer Series in Operations Research and Financial Engineering* (Springer, Berlin).

Pérez-Liva, M., Herraiz, J. L., Udías, J. M., Miller, E., Cox, B. T., and Treeby, B. E. (**2017**). "Time domain reconstruction of sound speed and

attenuation in ultrasound computed tomography using full wave inversion," J. Acoust. Soc. Am. **141**(3), 1595–1604.

Pratt, R., Huang, L., Duric, N., and Littrup, P. (**2007**). "Sound-speed and attenuation imaging of breast tissue using waveform tomography of transmission ultrasound data," *Proceedings of SPIE - The International Society for Optical Engineering*, Vol. 6510.

Ranger, B., Littrup, P., Duric, N., Li, C., Schmidt, S., Lupinacci, J., Myc, L., Szczepanski, A., Rama, O., and Bey-Knight, L. (**2010**). "Breast imaging with ultrasound tomography: A comparative study with MRI," in *Medical Imaging 2010: Ultrasonic Imaging, Tomography, and Therapy*, edited by J. D'hooge and S. A. McAleavey (International Society for Optics and Photonics, SPIE), Vol. 7629, pp. 50–58.

Ravasi, M., and Vasconcelos, I. (**2020**). "PyLops—A linear-operator Python library for scalable algebra and optimization," SoftwareX **11**, 100361.

Rickett, J., and Fomel, S. (**1999**). "A second-order fast marching eikonal solver," SEP Rep. **100**, 287–292.

Roy, O., Schmidt, S., Li, C., Allada, V. S. V. P., West, E., Kunz, D., and Duric, N. (**2013**). "Breast imaging using ultrasound tomography: From clinical requirements to system design," in *2013 IEEE International Ultrasonics Symposium (IUS)*, pp. 1174–1177.

Ruiter, N. V. (**2016**). "Dreidimensionale ultraschall-computertomographie: vom konzept zur klinischen anwendung" ("Three-dimensional ultrasound computed tomography: From concept to clinical application"), Karlsruher Institut für Technologie, 54.02.02; LK 01.

Ruiter, N. V., Hopp, T., Zapf, M., Menshikov, A., Kaiser, C., and Gemmeke, H. (**2018**). "3d ultrasound computer tomography for breast cancer diagnosis at kit: An overview," in *Proceedings of the International Workshop on Medical Ultrasound Tomography*, 1–3 November, Speyer, Germany (KIT Scientific Publishing, Karlsruher), pp. 205–216.

Sabra, K. G., Gerstoft, P., Roux, P., and Kuperman, W. A. (**2005**). "Surface wave tomography from microseisms in Southern California," Geophys. Res. Lett. **32**, L14311, https://doi.org/10.1029/2005GL023155.

Sager, K., Ermert, L., Boehm, C., and Fichtner, A. (**2018**). "Towards full waveform ambient noise inversion," Geophys. J. Int. **212**, 566–590.

Sandhu, G., Li, C., Roy, O., Schmidt, S., and Duric, N. (**2015**). "Frequency domain ultrasound waveform tomography: Breast imaging using a ring transducer," Phys. Med. Biol. **60**, 5381–5398.

Saygin, E., and Kennett, B. L. N. (**2012**). "Crustal structure of Australia from ambient seismic noise tomography," J. Geophys. Res. **117**, B01304, https://doi.org/10.1029/2011JB008403.

Schickert, M. (**2005**). "Progress in ultrasonic imaging of concrete," Mat. Struct. **38**, 807–815.

Schimmel, M., and Paulssen, H. (**1997**). "Noise reduction and detection of weak, coherent signals through phase-weighted stacks," Geophys. J. Int. **130**, 497–505.

Schimmel, M., Stutzmann, E., and Gallart, J. (**2011**). "Using instantaneous phase coherence for signal extraction from ambient noise data at a local to a global scale," Geophys. J. Int. **184**, 494–506.

Seidl, R., and Rank, E. (**2017**). "Full waveform inversion for ultrasonic flaw identification," AIP Conf. Proc. **1806**(1), 090013.

Sethian, J., and Popovici, A. (**1999**). "Three dimensional traveltimes computation using the fast marching method," Geophysics **64**, 516–523.

Sethian, J. A. (**1996**). "A fast marching level set method for monotonically advancing fronts," Proc. Natl. Acad. Sci. U.S.A. **93**(4), 1591–1595.

Shapiro, N., Campillo, M., Stehly, L., and Ritzwoller, M. (**2005**). "High-resolution surface-wave tomography from ambient seismic noise," Science **307**, 1615–1618.

Stehly, L., Fry, B., Campillo, M., Shapiro, N. M., Guilbert, J., Boschi, L., and Giardini, D. (**2009**). "Tomography of the Alpine region from observations of seismic ambient noise," Geophys. J. Int. **178**, 338–350.

Ulrich, I. E., Boehm, C., Zunino, A., Bösch, C., and Fichtner, A. (**2022**). https://mybinder.org/v2/gl/swp_ethz\%2Fpublic\%2Frandom-field-interferometry/master (Last viewed 5/25/2022).

Ulrich, I. E., Zunino, A., Boehm, C., and Fichtner, A. (**2021**). "Sparsifying regularizations for stochastic sample average minimization in ultrasound computed tomography," in *Medical Imaging 2021: Ultrasonic Imaging and Tomography*, edited by B. C. Byram and N. V. Ruiter (International Society for Optics and Photonics, SPIE), Vol. 11602, pp. 194–209.

VanDecar, J. C., and Crosson, R. S. (**1990**). "Determination of teleseismic relative phase arrival times using multi-channel cross-correlation and least squares," Bull. Seis. Soc. Am. **80**, 150–169.

Vogel, C. R. (**2002**). *Computational Methods for Inverse Problems* (Society for Industrial and Applied Mathematics, Philadelphia).

Wapenaar, K. (**2003**). "Synthesis of an inhomogeneous medium from its acoustic transmission response," Geophys. **68**, 1756–1759.

Wapenaar, K., and Fokkema, J. (**2006**). "Green's function representations for seismic interferometry," Geophysics **71**(4), SI33–SI46.

Weaver, R. L., and Lobkis, O. I. (**2004**). "Diffuse fields in open systems and the emergence of Green's function," J. Acoust. Soc. Am. **116**, 2731–2734.